

Manuscript version: Author's Accepted Manuscript

The version presented in WRAP is the author's accepted manuscript and may differ from the published version or Version of Record.

Persistent WRAP URL:

<http://wrap.warwick.ac.uk/143879>

How to cite:

Please refer to published version for the most recent bibliographic citation information. If a published version is known of, the repository item page linked to above, will contain details on accessing it.

Copyright and reuse:

The Warwick Research Archive Portal (WRAP) makes this work by researchers of the University of Warwick available open access under the following conditions.

© 2020 Elsevier. Licensed under the Creative Commons Attribution-NonCommercial-NoDerivatives 4.0 International <http://creativecommons.org/licenses/by-nc-nd/4.0/>.



Publisher's statement:

Please refer to the repository item page, publisher's statement section, for further information.

For more information, please contact the WRAP Team at: wrap@warwick.ac.uk.

Testing of stainless steel I-section columns in fire

Zhe Xing^{a,*}, Ou Zhao^b, Merih Kucukler^c, Leroy Gardner^a

^a*Department of Civil and Environmental Engineering, Imperial College London, London SW7 2AZ, UK*

^b*School of Civil and Environmental Engineering, Nanyang Technological University, Singapore*

^c*School of Engineering, University of Warwick, Coventry, CV4 7AL, UK*

Abstract

Although there have been significant developments in the testing, simulation and design of stainless steel structural elements at room temperature, the structural response of stainless steel members in fire has received significantly less attention. In particular, full-scale fire tests on stainless steel I-section members, which are becoming increasingly widely used in structural engineering applications to meet growing load-carrying capacity demands, are currently scarce. In this paper, the results of eight full-scale anisothermal fire tests on grade 1.4301 laser-welded austenitic stainless steel I-section columns are reported. Complementary initial local and global geometric imperfection measurements, room temperature tensile coupon tests and room temperature column buckling tests are also described. On the basis of the findings from the fire experiments, the accuracy and safety of the European fire design standard EN 1993-1-2 and the recent design recommendations of [1] for stainless steel columns in fire, which will be incorporated into the upcoming version of EN 1993-1-2, are assessed. It is observed that, relative to the existing column fire design rules in EN 1993-1-2, the design method of [1] provides more reliable ultimate strength predictions for austenitic stainless steel I-section columns in fire.

Keywords: Anisothermal; Buckling; Fire tests; Fire design; I-section; Laser-welded; Stainless steel

1. Introduction

Austenitic stainless steel displays superior strength and stiffness retention in comparison to carbon steel at elevated temperatures, resulting in enhanced structural performance in fire [2]. This, coupled with sound mechanical properties, high ductility and excellent durability, has led to stainless steel to be increasingly utilised in structural and offshore applications [3–5]. A number of studies into the structural stability of stainless steel members in fire has been performed [6–11], but experimental data on stainless steel structural members under fire conditions are rather limited [12–15]. This is particularly the case for stainless steel I-section members, which are being increasingly utilised to fulfil higher load-carrying capacity requirements in stainless steel structures

*Corresponding author

Email addresses: zhe.xing16@imperial.ac.uk (Zhe Xing), ou.zhao@ntu.edu.sg (Ou Zhao), merih.kucukler@warwick.ac.uk (Merih Kucukler), leroy.gardner@imperial.ac.uk (Leroy Gardner)

[16]. Gardner et al. [17] conducted one anisothermal (transient-state) fire test on a grade 1.4301 austenitic stainless steel I-section column. More recently, Ding et al. [18] and Liu et al. [19] carried out seven anisothermal fire column tests on grade 1.4301 austenitic stainless steel I-section members in which the specimens were axially or axially and rotational restrained. However, in the fire tests of [18, 19], the critical temperatures of the specimens only ranged between 520 °C and 640 °C; full-scale fire tests on austenitic stainless steel I-section columns covering a broader range of failure temperatures are necessary to investigate their elevated temperature response comprehensively.

To this end, eight full-scale fire tests have been performed on laser-welded grade 1.4301 austenitic stainless steel I-section columns and are presented in this paper. In addition to the fire tests, two room temperature tests on columns with the same geometric properties and from the same batch of material as those of the specimens subjected to fire testing have also been conducted. In the fire tests carried out in this study, the critical temperatures of the specimens ranged between approximately 300 °C and 800 °C, thereby covering the full practical range of fire design temperatures. The anisothermal testing method was adopted in the experiments to mimic a real fire situation. In this method, axial compression is first applied to the test specimen, and then the specimen is heated at a predefined heating rate until failure. The experimental results for the ten austenitic stainless steel columns, covering two cross-sections and four different axial load levels, are reported in addition to tensile coupon tests at room temperature and initial geometric imperfection measurements made on the specimens. Using the results of the fire tests, the accuracy and safety of EN 1993-1-2 [20] and the recent design proposals of Kucukler et al. [1], which will be implemented in the upcoming version of the European fire design standard EN 1993-1-2, are assessed for the design of stainless steel I-section columns at elevated temperatures.

2. Material properties

The tested I-section members were fabricated through the laser-welding of hot-rolled grade 1.4301 austenitic stainless steel plates; the laser-welding was carried out to Class B quality level for weld imperfections according to EN ISO 13919-1 [21]. The chemical compositions and material properties of the tested I-section members, as provided in the manufacturer's mill certificates, are summarised in Tables 1 and 2 respectively, where $f_{y, \text{mill}}$ is the 0.2% proof stress, $f_{p1.0, \text{mill}}$ is the 1% proof stress, $f_{u, \text{mill}}$ is the ultimate tensile stress and $\varepsilon_{f, \text{mill}}$ is the strain at fracture measured over the gauge length of $5.65 \sqrt{S_0}$, where S_0 is the cross-sectional area of the coupon extracted. Two cross-section sizes were employed for the column test specimens for: I-198×99×4.5×7 and I-248×124×5×8. The labelling system of the cross-sections in Table 2 is based on the cross-section dimensions shown in Fig. 1 - i.e. I-198×99×4.5×7 indicates an I-section with a cross-section nominal depth h of 198 mm, flange width b of 99 mm, web thickness t_w of 4.5 mm and flange thickness t_f of 7 mm.

In this study, a total of eight tensile coupons were extracted from the two tested cross-section shapes. As shown in Fig. 1, two tensile coupons were cut from the top and bottom flanges and the other two were cut from the web of each cross-section. Fig. 2 shows the dimensions of the tensile coupons, which are in accordance with the recommendations of [22]. All of the coupon tests were performed using a 250 kN hydraulic testing machine under a displacement-controlled

loading scheme; the initial loading rate was 0.05 mm/min, and once the nominal yield stress had been reached, the loading rate was increased to 0.8 mm/min until the fracture. The tensile coupon test setup is illustrated in Fig. 3, where it can be seen that an extensometer was mounted onto the middle of the coupons and two strain gauges were adhered to the mid-height of the two sides of the coupons. The coupons were labelled with respect to the nominal thickness of the plate from which they were extracted and whether they were extracted from the web or flange plate of a cross-section. An additional number (i.e. 1 or 2) was also used to label the coupons since two coupons were extracted from each web and flange plate. Thus, TC4.5-W-1 corresponds to one of the two tensile coupons extracted from a web plate with a nominal thickness of 4.5 mm. The measured stress-strain curves from the eight tensile coupons are plotted in Fig. 4a–4d and the key material properties are reported in Table 3, where t is the coupon thickness, E is the Young's modulus, f_y is 0.2% proof stress, $f_{p1.0}$ is the 1% proof stress, $f_{2.0}$ is the stress at 2% total strain, f_u is the ultimate stress, ε_u is the ultimate strain and ε_f is the fracture strain measured over a 50 mm gauge length. The Ramberg-Osgood exponents n and m_u [23–26] in Table 3 were obtained by fitting the two-stage compound Ramberg–Osgood material model presented in [3] and given by eq. (1) and eq. (2) to the stress-strain ($\sigma - \varepsilon$) curves obtained from the coupon tests. Note that in eq. (2), $E_{p0.2}$ and $\varepsilon_{p0.2}$ are the tangent modulus and total strain at the 0.2% proof stress, respectively.

$$\varepsilon = \frac{\sigma}{E} + 0.002 \left(\frac{\sigma}{f_y} \right)^n \quad \text{for } \sigma \leq f_y \quad (1)$$

$$\varepsilon = \frac{\sigma - f_y}{E_{p0.2}} + \left(\varepsilon_u - \varepsilon_{p0.2} - \frac{f_u - f_y}{E_{p0.2}} \right) \left(\frac{\sigma - f_y}{f_u - f_y} \right)^{m_u} + \varepsilon_{p0.2} \quad \text{for } f_y < \sigma \leq f_u, \quad (2)$$

For the numerical simulation of the elevated temperature response of stainless steel elements, the modified two-stage compound Ramberg–Osgood material model [1, 27, 28] can also be used to represent their elevated temperature material stress-strain response, as given by eqs. (3) and (4):

$$\varepsilon = \frac{\sigma}{E_\theta} + 0.002 \left(\frac{\sigma}{f_{p0.2,\theta}} \right)^{n_\theta} \quad \text{for } \sigma \leq f_{p0.2,\theta} \quad (3)$$

$$\varepsilon = \frac{\sigma - f_{p0.2,\theta}}{E_{p0.2,\theta}} + \left(\varepsilon_{u,\theta} - \varepsilon_{p0.2,\theta} - \frac{f_{u,\theta} - f_{p0.2,\theta}}{E_{p0.2,\theta}} \right) \left(\frac{\sigma - f_{p0.2,\theta}}{f_{u,\theta} - f_{p0.2,\theta}} \right)^{m_\theta} + \varepsilon_{p0.2,\theta} \quad \text{for } f_{p0.2,\theta} < \sigma \leq f_{u,\theta}, \quad (4)$$

where n_θ and m_θ are strain hardening exponents, $f_{p0.2,\theta}$ is the 0.2% proof strength at temperature θ , E_θ is the modulus of elasticity at temperature θ , $E_{p0.2,\theta}$ and $\varepsilon_{p0.2,\theta}$ are the tangent modulus and total strain corresponding to $f_{p0.2,\theta}$, and $f_{u,\theta}$ and $\varepsilon_{u,\theta}$ are the ultimate tensile strength and strain at temperature θ . As recommended in [27], the elevated temperature Ramberg-Osgood exponents n_θ and m_θ can be taken equal to the corresponding exponents n and m used in the room temperature material model (i.e. $n_\theta = n$, $m_\theta = m$) leading to accurate predictions of the roundedness of the elevated temperature stress-strain curves of stainless steel. Alternatively, m_θ can also be calculated using the expression given in [1, 28, 29] to ensure that the second stage of the Ramberg-Osgood material model passes through the elevated temperature strengths at 2% total strain $f_{2,\theta}$ and the

ultimate strain $f_{u,\theta}$ exactly at 2% total strain and the ultimate strain $\varepsilon_{u,\theta}$, respectively. The elevated temperature material properties of stainless steel (i.e. $f_{p0.2,\theta}$, $f_{2,\theta}$, E_θ , $f_{u,\theta}$ and $\varepsilon_{u,\theta}$) can be estimated by multiplying the strength ($k_{p0.2,\theta}$, $k_{2,\theta}$), stiffness ($k_{E,\theta}$) and ductility ($k_{\varepsilon_{u,\theta}}$) reduction factors given in [27] (see Fig. 5), which are based on extensive material test results [30-32], by the corresponding room temperature material properties, i.e. $f_{p0.2,\theta} = k_{p0.2,\theta}f_y$, $f_{2,\theta} = k_{2,\theta}f_y$, $E_\theta = k_{E,\theta}E$, $f_{u,\theta} = k_{u,\theta}f_u$ and $\varepsilon_{u,\theta} = k_{\varepsilon_{u,\theta}}\varepsilon_u$. The full elevated temperature stress-strain curves can be generated using eqs. (3) and (4) in conjunction with the measured room temperature properties and the reduction factors from [27], as shown for the 8 mm thick material examined herein in Fig. 6.

3. Geometry and imperfection measurements

Prior to conducting the column tests, the geometric properties of the ten tested specimens were measured; the measurements are summarised in Table 4, where L is the buckling length of the columns between the two centres of the knuckle bearings used in the tests, as shown in Fig. 7. The column specimens were labelled considering their cross-section profiles: LC1 corresponds to the column specimens with the I-248×124×5×8 cross-section, while LC2 corresponds to the column specimens with the I-198×99×4.5×7 cross-section. An additional number was also utilised in the labelling of the column specimens to signify the four different nominal axial load ratios $n_r = 0.6, 0.5, 0.4$ and 0.3 , which are equal to the ratio of the applied axial load $N_{Ed,test}$ to the room temperature minor axis flexural buckling resistances N_u determined from the room temperature column buckling tests (i.e. $n_r = N_{Ed,test}/N_u$). The column specimens tested at room temperature were denoted LC1-20C for the column with the I-248×124×5×8 cross-section and LC2-20C for the column with the I-198×99×4.5×7 cross-section.

Initial local geometric imperfections of four columns (LC1-20C, LC1-0.6, LC2-20C and LC2-0.6) and initial global geometric imperfections of all tested columns were measured following the procedure recommended in [33]. For the local imperfection measurements, the columns were first secured to the bed of a CNC milling machine, and then an LVDT, which was attached to the movable frame of the CNC milling machine, was moved along a 600 mm length away from the ends of the specimens to record displacements at 1 mm intervals, as shown in Fig. 8; lines of measurements were taken at the nine different locations illustrated in Fig. 9. Fig. 10a shows a typical measured local geometric imperfection distribution. The measured web local imperfection magnitudes w_w and the measured flange local imperfection magnitudes w_f , which are provided in Table 4, were defined as the maximum deviations from a straight line fitted to the local imperfection measurements along the specimen lengths using least squares regression. As can be seen from Table 4, both the measured web w_w and flange local imperfections w_f were significantly lower than the manufacturing tolerance of 1/100 of the web height and 1/100 of the flange width set out in EN 1090-2 [34].

In the measurement of the initial global geometric imperfection magnitudes, the LVDT was moved to record deviations at Location 5 of the cross-sections (see Fig. 9) along the full lengths L_c of the specimens with the exception of two 100 mm lengths at the ends of the columns due to the limited range of the movable frame of the CNC milling machine. Fig. 10b shows a typical measured initial global geometric imperfection distribution where the maximum deviation from a straight line connecting the ends of the measured length of the column was taken as the max-

imum global geometric imperfection v_0 . The measured global geometric imperfections for each specimen are provided in Table 4, where it can be seen that the average of the measured global geometric imperfection magnitudes was around $1/7000$ of the specimen lengths L_c (i.e. $L_c/7000$), which is significantly lower than the manufacturing tolerance of $L_c/1000$ set out in EN 1090-2 [34].

4. Column tests at room temperature

To provide a benchmark against which to assess the influence of fire conditions on the structural response of the examined stainless steel I-section columns, two corresponding room temperature minor axis flexural buckling tests were performed. The columns were tested with pinned end conditions in a horizontal self-reacting test rig, which was also utilised in the fire tests. The nominal geometries of the two specimens were identical to those of the columns tested in fire: (i) a column with an I-248×124×5×8 cross-section and a buckling length L of 2.5 m and (ii) a column with an I-198×99×4.5×7 cross-section and a buckling length L of 2.75 m.

4.1. Test setup and testing procedures

Fig. 7 shows the overall experimental apparatus, which consisted of a 5000 kN capacity horizontal self-reacting test rig with hydraulic actuator to apply the axial load, knuckle bearings at the ends of the column to provide pin-ended support conditions about the minor axis, four LVDTs placed at four corners of the right hand end plate to measure the end rotations and one string transducer attached to the mid-height of the column to measure the mid-height lateral deformations. The furnace was retained in situ but left open during the room temperature testing. Fig. 11 shows the details of the loading system at the left hand end of the column, where a load cell, placed between the actuator and the left hand knuckle bearing, was used for measuring the applied loading. Before testing, a laser leveller was utilised to verify the alignment of the actuator, the load cell, the pins of the two knuckle bearings and the column.

Member bow imperfections v_0 were measured using the setup shown in Fig. 9 prior to testing and found to have an average magnitude of about $L/7000$; additional loading eccentricities e_0 were introduced by eccentrically welding the specimens to their end plates, as shown in Fig. 12, such that the total (downward) global imperfection ($v_0 + e_0$) was approximately $L/1000$. The actual measured total global imperfection amplitudes were back-calculated using four strain gauges affixed to the specimens at mid-height at a distance of $d_s = 10$ mm from the outer edges of the four flanges, following the method described in [35, 36]. The calculation of the actual total global imperfection amplitude ($v_0 + e_0$) was performed using eqs. (5)–(7):

$$v_0 + e_0 = \frac{EI_z(\varepsilon_{\max} - \varepsilon_{\min})}{N(b_f - 2d_s)} - \delta, \quad (5)$$

in which

$$\varepsilon_{\max} = (\varepsilon_1 + \varepsilon_2)/2, \quad (6)$$

$$\varepsilon_{\min} = (\varepsilon_3 + \varepsilon_4)/2, \quad (7)$$

where $\varepsilon_1, \varepsilon_2, \varepsilon_3$ and ε_4 are the strain gauge readings, E is the modulus of elasticity, I_z is the minor axis second moment of area, N is the applied load and δ is the mid-height lateral deflection. The locations of the four strain gauges are illustrated in Fig. 13.

Table 5 summarises the measured total test global imperfection values, which comprised two parts: (i) the initial global imperfection v_0 and (ii) the additional loading eccentricity e_0 introduced in each test. In the two room temperature column tests, a displacement-controlled loading scheme was utilised and the axial loading was applied at a rate of 0.3 mm/min. All the data, including the applied load, the mid-height deflection, the strains measured by the four strain gauges and the displacements of the four LVDTs, were recorded by a data logger at 1 s intervals.

4.2. Test results

As anticipated, both of the tested stainless steel columns (LC1-20C and LC2-20C) failed by minor axis flexural buckling; a typical failure mode, that of LC2-20C, is shown in Fig. 14. The load versus mid-height lateral displacement curves for the tested columns are plotted in Fig. 15. The key results from the tests – the minor axis flexural buckling loads N_u and the lateral mid-height displacements and end-rotations at failure – are summarised in Table 5.

5. Column fire tests

A total of eight fire tests were carried out on pin-ended stainless steel I-section columns. Of these eight tested columns, four had an I-248×124×5×8 cross-section with a buckling length of 2.5 m and the other four had an I-198×99×4.5×7 cross-section with a buckling length of 2.75 m. An anisothermal testing method was employed in all fire tests. Four different load ratios n_r equal to the ratio of the applied axial load $N_{Ed, test}$ to the minor axis flexural buckling capacities N_u (i.e. $n_r = N_{Ed, test}/N_u$) obtained from the room temperature tests, namely $n_r = 0.3, 0.4, 0.5$ and 0.6 , were considered to achieve a broad range of failure temperatures.

5.1. Test setup

Fig. 16 shows the column fire test setup, which consisted of a 5000 kN capacity horizontal self-reacting test rig with an actuator, an electric furnace, an LVDT with a bespoke displacement measurement system to measure the lateral deflection of the column at mid-height and four strain gauges to determine the total test eccentricity. Note that a length of 115 mm for the LC1 specimens and a length of 240 mm for the LC2 specimens were left outside the furnace at the two ends, which remained unheated during the testing; this was because the knuckle bearings connected to the end plates of the columns had to be placed outside the furnace and required space to rotate. Before the testing, the left hand and right hand openings of the furnace were heavily insulated around the columns by heat resistant fabrics and rockwool to avoid any heat loss.

The electric furnace shown in Fig. 17 was used for the column fire tests. During testing, the air temperature of the furnace, which was measured through two thermocouples, was increased in accordance with the ISO-834 standard fire curve [37] as shown in Fig. 18. One of the thermocouples was connected to the furnace heating control system and the other thermocouple was embedded into a furnace wall (see Fig. 19). In addition to these two thermocouples, there were seven thermocouples attached to the columns at a series of points along their lengths to capture

the surface temperature distribution; the locations of the thermocouples are illustrated in Fig. 20, where thermocouple 1 and 7 were used for measuring the temperature of the two parts of the specimens outside the furnace.

Fig. 21 shows the LVDT used to measure the mid-height lateral deflection of the column specimens; the LVDT was installed above the furnace and covered with heat resistant fabric. The uncovered extension rod of the LVDT was connected to the bespoke displacement measurement system shown in Fig. 17 using an Alsint 99.7 rod. Alsint 99.7 has a high yield strength (300 MPa) and a low coefficient of thermal expansion ($7.8 \times 10^{-6} \text{ K}^{-1}$). The Alsint 99.7 rod, one end of which was connected to the extension rod of the LVDT and the other end of which was attached to the surface of the column, was able to move vertically with the extension rod of the LVDT to measure the lateral deflection of the columns at the mid-height.

5.2. Testing procedure

In the fire tests, the axial load $N_{\text{Ed,test}}$ was first applied to the specimens through the horizontal self-reacting test rig under displacement control at a rate of 0.3 mm/min. Once the predefined axial load ratio $n_r = N_{\text{Ed,test}}/N_u$ equal to ratio of the applied axial load $N_{\text{Ed,test}}$ to the room temperature minor axis flexural buckling capacity N_u of the specimen, testing was switched to load control and the load was held constant for fifteen minutes. Note that the room temperature minor axis flexural buckling capacities N_u were taken as the ultimate loads obtained for the LC1-20C and LC2-20C columns from the room temperature tests, which are described in Section 4. The air temperature in the furnace was then increased following the ISO-834 standard fire curve until the axial load applied to the column $N_{\text{Ed,test}}$ could no longer be sustained. During the heating process, the column was allowed to expand in order to keep the predefined axial load ratio constant. The applied axial compression values $N_{\text{Ed,test}}$, load ratios n_r and measured total eccentricities of the eight tested stainless steel columns are reported in Table 6.

5.3. Test results

All the tested columns failed by minor axis flexural buckling. Fig. 22 shows the typical failure modes of the columns with different axial load ratios n_r , where surface colour changes associated with the different failure temperatures are clearly evident. In this subsection, additional details with respect to the temperature distributions in the tested specimens and the behaviour of the tested stainless steel columns observed during the experiments are presented.

5.3.1. Temperature distributions

The measured furnace air temperature versus time relationships in the eight column tests are shown in Fig. 23a–23b together with the ISO-834 standard fire curve [37]. As can be seen from the figures, the air temperature in the furnace generally followed the trend of the ISO-834 standard fire curve [37] though lagged somewhat behind, particularly at the beginning of the experiments.

Fig. 24 shows the temperatures measured by the seven thermocouples attached to the surface of specimen LC2-0.3. In the figure, the temperature values measured by thermocouples 2–6 in the heated region increased following a similar trend with time. The temperatures of the two parts of the column outside the furnace were measured by thermocouple 1 and thermocouple 7, which remained at room temperature throughout the testing. Fig. 25a–25b show the average measured

column surface temperature-time relationships for all the fire tests, where the column surface temperatures are taken as the mean of the temperature values measured by the five thermocouples attached to the column surfaces in the heated regions. Table 7 provides a summary of the key experimental results for the eight stainless steel I-section column tests in fire, including the critical failure temperature $\theta_{cr,test}$ and the fire resistance in terms of the time duration $t_{fi,test}$ for which the columns were able to resist the pre-applied loads $N_{Ed,test}$. The fire resistance $t_{fi,test}$ and critical temperature $\theta_{cr,test}$ of a specimen was assumed to be reached when one of the two failure criteria provided in European Standard EN 1363-1 (2012) [38] was reached: (i) the maximum allowable axial contraction magnitude of $C = h/100$ mm or (ii) the maximum allowable axial contraction rate of $dC/dt = 3h/1000$ mm/min, where h is the initial column height in mm.

5.3.2. Behaviour of columns

In Fig. 26, the recorded axial deformation versus temperature paths for the eight stainless steel column tests in fire are shown. It can be seen that the columns initially shortened due to the applied axial loading $N_{Ed,test}$, and then started to expand with increasing temperature. When the column temperatures were below about 300 °C, it is seen from Fig. 26 that the measured axial expansion rates of the columns were smaller than those measured for high temperature levels. This was mainly because the column temperature increased rapidly to 300 °C and the position of the actuator, which was manually controlled to maintain a constant axial load, lagged slightly behind where it ought to have been. After 300 °C, the column temperature increased more slowly and all the columns expanded linearly with increasing temperature levels and behaved similarly prior to their failure.

Fig. 27 shows the recorded lateral mid-height deflection versus average surface temperature curves for the eight tested stainless steel I-section columns in fire. Note that the thermal expansion of the Alsint 99.7 rod, although small, was non-negligible (up to about 2 mm at 750 °C) and was hence calculated and removed from the measured mid-height lateral deflections of column specimens. As can be seen in the figure, the columns exhibited small lateral deflections under the initial axial loading; the lateral deflections of the columns then displayed small fluctuations owing to possible thermal bowing under increasing temperature. Finally, as the columns approached failure, the column stiffness reduced rapidly and there were significant increases in mid-height lateral deflections signifying flexural buckling about minor axis.

6. Accuracy of EN 1993-1-2 [20] and recent design recommendations of Kucukler et al. [1] for stainless steel I-section columns in fire

In this section, the accuracy and safety of the European steel fire design standard EN 1993-1-2 [20] and the design method of Kucukler et al. [1], which is due to be incorporated into the upcoming version of EN 1993-1-2 [20], are assessed for the ultimate strength predictions of stainless steel columns in fire, using the experimental results obtained in the previous section.

6.1. EN 1993-1-2 [20]

The current version of EN 1993-1-2 [20] states that the design buckling resistance $N_{b,fi,t,Rd}$ at time t of a stainless steel compression member at uniform temperature θ should be calculated as:

$$N_{b,fi,t,Rd} = \frac{\chi_{fi} A k_{2,\theta} f_y}{\gamma_{M,fi}} \quad \text{for Class 1,2 or 3 sections,} \quad (8)$$

$$N_{b,fi,t,Rd} = \frac{\chi_{fi} A_{eff} k_{p0.2,\theta} f_y}{\gamma_{M,fi}} \quad \text{for Class 4 sections,} \quad (9)$$

where A and A_{eff} are the gross cross-sectional area and the effective area respectively, $k_{2,\theta}$ and $k_{p0.2,\theta}$ are respectively the reduction factors for the strength at 2% total strain and 0.2% proof strength at temperature θ , f_y is the yield strength at room temperature, $\gamma_{M,fi}$ is the partial safety factor for fire design taken as 1.0 and χ_{fi} is the member buckling reduction factor determined by:

$$\chi_{fi} = \frac{1}{\phi_{\theta} + \sqrt{\phi_{\theta}^2 - \bar{\lambda}_{\theta}^2}}, \quad (10)$$

where

$$\phi_{\theta} = 0.5 \left[1 + \alpha \bar{\lambda}_{\theta} + \bar{\lambda}_{\theta}^2 \right] \text{ with } \alpha = 0.65 \sqrt{\frac{235}{f_y}}. \quad (11)$$

The elevated temperature non-dimensional column slenderness $\bar{\lambda}_{\theta}$ is calculated as:

$$\bar{\lambda}_{\theta} = \bar{\lambda} \sqrt{\frac{k_{2,\theta}}{k_{E,\theta}}} \quad \text{for Class 1,2 or 3 sections,} \quad (12)$$

$$\bar{\lambda}_{\theta} = \bar{\lambda} \sqrt{\frac{k_{p0.2,\theta}}{k_{E,\theta}}} \quad \text{for Class 4 sections,} \quad (13)$$

where $\bar{\lambda}$ is the non-dimensional slenderness at room temperature and $k_{E,\theta}$ is the Young's modulus reduction factor at temperature θ . A comparison of the pre-applied axial loads in the fire tests $N_{Ed,test}$ and the column buckling resistances according to EN 1993-1-2 [20] $N_{b,Rd,EC3}$ determined by considering the corresponding measured critical temperature θ_{cr} values for the specimens obtained from the tests is shown in Table 8. As can be seen from the table, all the ratios of $N_{Ed,test}$ to $N_{b,Rd,EC3}$ are less than 1.0, which indicates that all the column buckling resistance predictions $N_{b,Rd,EC3}$ determined using the current version of EN 1993-1-2 [20] are on the unsafe side compared to the results from the physical experiments carried on stainless steel I-section columns in this paper. This mirrors the findings presented in [1], which prompted the development of improved design rules; these new design rules [1] are assessed against the test results from the present study in the following subsection.

6.2. The design method proposed by Kucukler et al. [1]

In the column buckling design method proposed by Kucukler et al. [1], the design buckling resistance $N_{b,fi,t,Rd}$ at time t of a stainless steel compression member at uniform temperature θ is given by:

$$N_{b,fi,t,Rd} = \frac{\chi_{fi} A k_{2,\theta} f_y}{\gamma_{M,fi}} \quad \text{for non-slender sections,} \quad (14)$$

$$N_{b,fi,t,Rd} = \frac{\chi_{fi} A_{eff} k_{2,\theta} f_y}{\gamma_{M,fi}} \quad \text{for slender sections,} \quad (15)$$

in which

$$\chi_{fi} = \frac{1}{\phi_\theta + \sqrt{\phi_\theta^2 - \beta \bar{\lambda}_\theta^2}}, \quad (16)$$

where

$$\phi_\theta = 0.5 \left[1 + \alpha \bar{\lambda}_\theta + \beta \bar{\lambda}_\theta^2 \right] \quad \text{with } \alpha = \alpha_0 / \xi_\theta \text{ and } \xi_\theta = \sqrt{\frac{k_{2,\theta}}{k_{E,\theta}}}, \quad (17)$$

in which α_0 is the elevated temperature imperfection factor and β is an auxiliary coefficient, taken respectively as 0.9 and 1.5 for the minor axis flexural buckling of austenitic stainless steel columns, and ξ_θ is the elevated temperature strength-to-stiffness ratio reduction factor. The non-dimensional slenderness at temperature θ is calculated as:

$$\bar{\lambda}_\theta = \bar{\lambda} \sqrt{\frac{k_{2,\theta}}{k_{E,\theta}}}. \quad (18)$$

Note that only two classes of cross-section, referred to as ‘non-slender’ and ‘slender’ are used in the proposed design method [1, 28], and the formulae for the determination of the effective cross-sectional area A_{eff} are described in [28].

Table 9 provides a comparison between the pre-applied loads $N_{Ed,test}$ to the stainless steel columns in the fire tests and the column buckling resistances determined by the design method of [1] $N_{b,Rd,Prop}$ at the corresponding measured critical temperature values $\theta_{cr,test}$ of the specimens. As can be seen from the table, for the tested eight I-section stainless steel columns in this paper, the average value of the ratios of N_{test} to $N_{b,Rd,Prop}$ is 1.21 with a low level of scatter, implying that, in contrast with EN 1993-1-2 [20], the design method proposed by [1] provides consistent and safe-sided resistance predictions. Since the tested columns were not heated along their full lengths, the influence of partial heating on their response was investigated herein by means of a targetted finite element study, employing the same modelling approach as described in [1]. Note that the finite element models were analysed isothermally, whereby the columns were first heated to a specified temperature level and then loaded to failure; hence, the ultimate load-carrying capacities corresponded directly to the peak loads obtained in the simulations. Reference to the failure criteria set out in EN 1363-1 (2012) [38] for the anisothermal analysis of structural members at

elevated temperatures was therefore not required. Simulations of the tested columns were performed under fully-heated and partially-heated conditions, and the corresponding ultimate loads, $N_{u,FE,full-heated}$ and $N_{u,FE,part-heated}$, were determined. Table 10 summarises the numerical results obtained, which indicate that the column resistances increase by about 2% due to partial heating relative to full heating. Additional numerical simulations were performed to investigate the influence of self-weight on the ultimate resistances of the horizontally tested columns; the obtained ultimate column resistances are shown in Table 11, where $N_{u,FE,w}$ and $N_{u,FE,nw}$ are the ultimate column resistances with and without self-weight included, respectively. Note that all of the column models buckled downwards, in the same direction as both the imperfection and the self-weight deflection. Table 11 demonstrates that the elevated temperature column resistances decrease by approximately 1% owing to the influence of the self-weight. Thus, the average value of the ratios of the ultimate column resistances observed in the experiments to those determined through the design method of [1] $N_{Ed,test}/N_{b,Rd,Prop}$ can be assumed to be equal to 1.20 when the influence of partial heating and self-weight on the test resistances is removed; this is approximately in line with the results obtained during the comprehensive numerical assessment of the accuracy of the column design method in Kucukler et al. [1], noting that the design method [1] is somewhat conservative for the parameter range considered through testing in the present study. For the same parameter range, the average of the ratios of the ultimate resistances determined through finite element analyses $N_{Ed,FE}$ to those determined using the design method of [1] $N_{b,Rd,Prop}$ (i.e. $N_{Ed,FE}/N_{b,Rd,Prop}$) was equal to 1.16. Overall, therefore, the experiments presented herein confirm the accuracy of the previous finite element modelling and support the suitability of the developed design rules [1].

7. Conclusions

An experimental study on grade 1.4301 austenitic stainless steel I-section columns in fire has been presented in this paper. Material tests on tensile coupons extracted from the web and flange plates of the stainless steel column specimens were performed at room temperature; the corresponding elevated temperature material properties were inferred on the basis of the strength and stiffness reduction factors set out in [27, 30, 31]. Prior to the fire tests, two columns with the same geometrical properties as those subjected to fire testing were tested at room temperature to obtain their benchmark room temperature minor axis flexural buckling load N_u . Following the room temperature member tests, eight anisothermal stainless steel column fire tests were conducted, in which two cross-sections and two column buckling lengths were considered. Four axial load ratios n_r , equal to 0.3, 0.4, 0.5 and 0.6, were adopted to achieve a range of failure temperature values. The accuracy and safety of the provisions of EN 1993-1-2 [20] and the recently proposed method of [1] for the design of stainless steel columns at elevated temperatures were assessed using the obtained experimental results. It was found that the ultimate resistance predictions of EN 1993-1-2 [20] were consistently on the unsafe side, while the design method of [1] provides accurate and safe-sided predictions of the fire resistance of stainless steel columns. The experimental study carried out in this paper fills an important gap in knowledge on the behaviour of stainless steel I-section columns in fire, and the results have provided a further validation of the suitability of the newly developed design method of Kucukler et al. [1], which is due to be incorporated into the upcoming version of EN 1993-1-2 [20].

Acknowledgement

The authors would like to thank Kenny Lim for providing the test specimens for the project. The contributions of Toh Yau Meng, Cheng Weng Kong, Li Fali, Choi Siew Pheng and Lim Yong Cheng are gratefully acknowledged.

References

- [1] Kucukler, M., Xing, Z., Gardner, L.. Behaviour and design of stainless steel I-section columns in fire. *Journal of Constructional Steel Research* 2020;165,105890.
- [2] Gardner, L. and Ng, K.T.. Temperature development in structural stainless steel sections exposed to fire. *Fire Safety Journal* 2006;41(3):185-203.
- [3] Gardner, L.. Stability and design of stainless steel structures–Review and outlook. *Thin-Walled Structures* 2019;141:208–216.
- [4] Wang, F.C. and Han, L.H.. Analytical behavior of carbon steel-concrete-stainless steel double-skin tube (DST) used in submarine pipeline structure. *Marine Structures* 2019; 63:99–116.
- [5] Vila-Real, P., Lopes, N., da Silva, L.S. and Franssen, J.M.. Lateral–torsional buckling of stainless steel I-beams in case of fire. *Journal of Constructional Steel Research* 2008;64(11):1302-1309.
- [6] Gardner, L.. Stainless steel structures in fire. *Proceedings of the Institution of Civil Engineers-Structures and Buildings* 2007;160(3):129–138.
- [7] Ng, K.T. and Gardner, L.. Buckling of stainless steel columns and beams in fire. *Engineering Structures* 2007;29(5):717–730.
- [8] Uppfeldt, B., Ala-Outinen, T. and Veljkovic, M.. A design model for stainless steel box columns in fire. *Journal of Constructional Steel Research* 2008;64(11):1294–1301.
- [9] To, E.C.Y. and Young, B.. Performance of cold-formed stainless steel tubular columns at elevated temperatures. *Engineering Structures* 2008;30(7):2012–2021.
- [10] Lopes, N., Vila-Real, P., da Silva, L. and Franssen, J.M.. Axially loaded stainless steel columns in case of fire. *Journal of Structural Fire Engineering* 2010;1(1):43-60.
- [11] Mohammed, A. and Afshan, S.. Numerical modelling and fire design of stainless steel hollow section columns. *Thin-Walled Structures* 2019;144,106243.
- [12] Ala-Outinen, T., Oksanen, T.. Stainless steel compression members exposed to Fire. *Research Notes 1864, Technical Research Centre of Finland (VTT), Finland; 1997.*
- [13] Tondini, N., Rossi, B. and Franssen, J.M.. Experimental investigation on ferritic stainless steel columns in fire. *Fire Safety Journal* 2013;62:238–248.
- [14] Fan, S., Ding, X., Sun, W., Zhang, L. and Liu, M., Experimental investigation on fire resistance of stainless steel columns with square hollow section. *Thin-Walled Structures* 2016;98:196–211.
- [15] Fan, S., Liu, M., Sun, W., Guo, Y. and Han, Y.L.. Experimental investigation of eccentrically compressed stainless steel columns with constraints in fire. *Fire Safety Journal* 2018;99:49–62.
- [16] Kucukler, M., Gardner, L., Bu, Y.. Flexural-torsional buckling of stainless steel I-section beam-columns: Testing, numerical modelling and design. *Thin-Walled Structures* 2020;150,16572.
- [17] Gardner, L., Baddoo, N.. Fire testing and design of stainless steel structures. *Journal of Constructional Steel Research* 2006;62:532–543.
- [18] Ding, R., Fan, S., Chen, G., Li, C., Du, E. and Liu, C.. Fire resistance design method for restrained stainless steel H-section columns under axial compression. *Fire Safety Journal* 2019;108,102837.
- [19] Liu, M., Fan, S., Ding, R., Chen, G., Du, E. and Wang, K.. Experimental investigation on the fire resistance of restrained stainless steel H-section columns. *Journal of Constructional Steel Research* 2019;163,105770.
- [20] EN 1993-1-2, Eurocode 3 Design of Steel Structures–Part 1-2: General Rules–Structural Fire Design. European Committee for Standardization (CEN), Brussels; 2005.
- [21] EN ISO 13919-1. Welding: electrons and laser beam welded joints – guidance on quality levels for imperfections – part 1: steel. European Committee for Standardization (CEN), Brussels; 1997.
- [22] Huang, Y. and Young, B.. The art of coupon tests. *Journal of Constructional Steel Research* 2014;96:159–175.

- [23] Mirambell, E. and Real, E.. On the calculation of deflections in structural stainless steel beams: An experimental and numerical investigation. *Journal of Constructional Steel Research* 2000;54(1):109–133.
- [24] Rasmussen, K.J.. Full-range stress–strain curves for stainless steel alloys. *Journal of Constructional Steel Research* 2003;59(1):47–61.
- [25] Gardner, L. and Yun, X.. Description of stress-strain curves for cold-formed steels. *Construction and Building Materials* 2018;189:527–538.
- [26] Arrayago, I., Real, E. and Gardner, L.. 2015. Description of stress-strain curves for stainless steel alloys. *Materials and Design* 2015;87:540–552.
- [27] Design manual for structural stainless steel, Fourth Edition, Steel Construction Institute (SCI);2017.
- [28] Xing, Z., Kucukler, M., Gardner, L.. Local buckling of stainless steel plates in fire. *Thin-Walled Structures* 2020;148,106570.
- [29] Liang, Y., Manninen, T., Zhao, O., Walport, F. and Gardner, L.. Elevated temperature material properties of a new high-chromium austenitic stainless steel. *Journal of Constructional Steel Research* 2019;152:261–273.
- [30] Gardner, L., Insausti, A., Ng, K.T. and Ashraf, M.. Elevated temperature material properties of stainless steel alloys. *Journal of Constructional Steel Research* 2010;66(5):634–647.
- [31] Gardner, L., Bu, Y., Francis, P., Baddoo, N.R., Cashell, K.A. and McCann, F.. Elevated temperature material properties of stainless steel reinforcing bar. *Construction and Building Materials* 2016;114:977–997.
- [32] Chen, J. and Young, B.. Stress–strain curves for stainless steel at elevated temperatures. *Engineering Structures* 2006;28(2):229–239.
- [33] Schafer, B.W. and Peköz, T.. Computational modeling of cold-formed steel: characterizing geometric imperfections and residual stresses. *Journal of Constructional Steel Research* 1998;47(3):193–210.
- [34] EN 1090-2, Execution of steel structures and aluminium structures. Part 2: technical requirements for steel structures. European Committee for Standardization (CEN), Brussels; 2018.
- [35] Zhao O, Rossi B, Gardner L, Young B.. Behaviour of structural stainless steel cross-sections under combined loading – part I: experimental study. *Engineering Structures* 2015;89:236–46.
- [36] Bu, Y. and Gardner, L.. Laser-welded stainless steel I-section beam-columns: Testing, simulation and design. *Engineering Structures* 2019;179:23–36.
- [37] ISO 834, Fire resistance tests–Elements of building construction, International Organization for Standards, Geneva; 2014.
- [38] EN 1363-1, Fire resistance tests: Part 1–General requirements. European Committee for Standardization (CEN);2012.

8. Figures

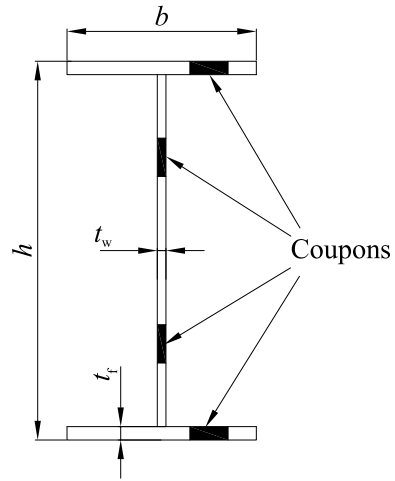


Figure 1: Cross-section labelling system and locations of tensile coupons

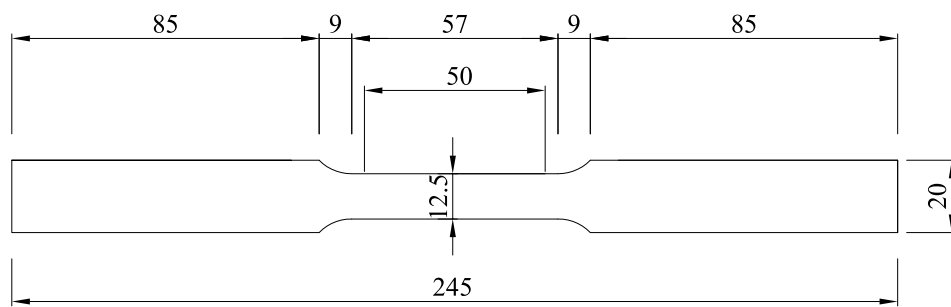


Figure 2: Dimensions of tensile coupon (dimensions in mm)

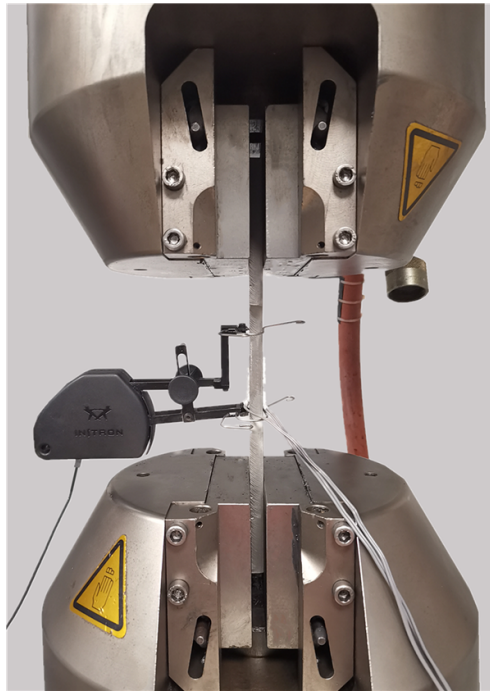
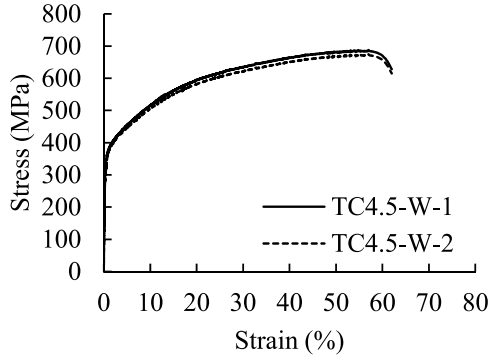
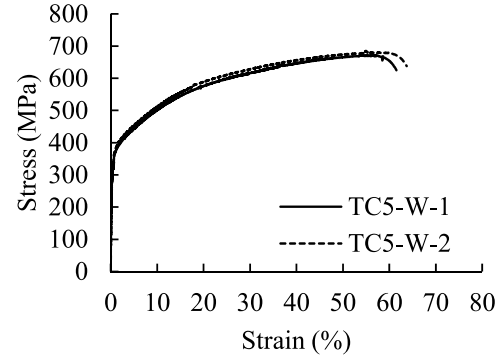


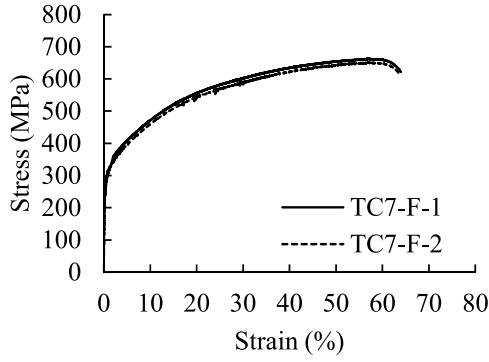
Figure 3: Tensile coupon test setup



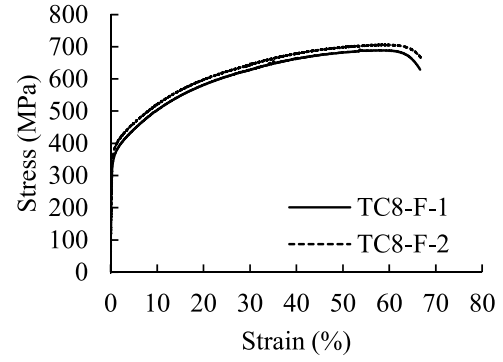
(a) Tensile coupon with 4.5 mm thickness (web)



(b) Tensile coupon with 5 mm thickness (web)



(c) Tensile coupon with 7 mm thickness (flange)



(d) Tensile coupon with 8 mm thickness (flange)

Figure 4: Tensile coupon test results at room temperature

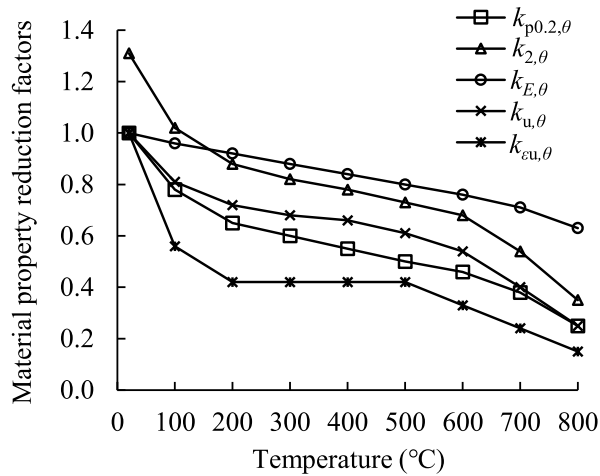


Figure 5: Strength ($k_{p0.2,\theta}$, $k_{2,\theta}$), stiffness ($k_{E,\theta}$) and ductility ($k_{\epsilon u,\theta}$) reduction factors of grade 1.4301 austenitic stainless steel at elevated temperatures from [27]

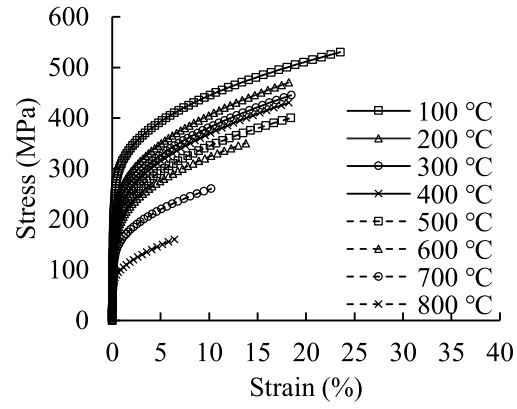
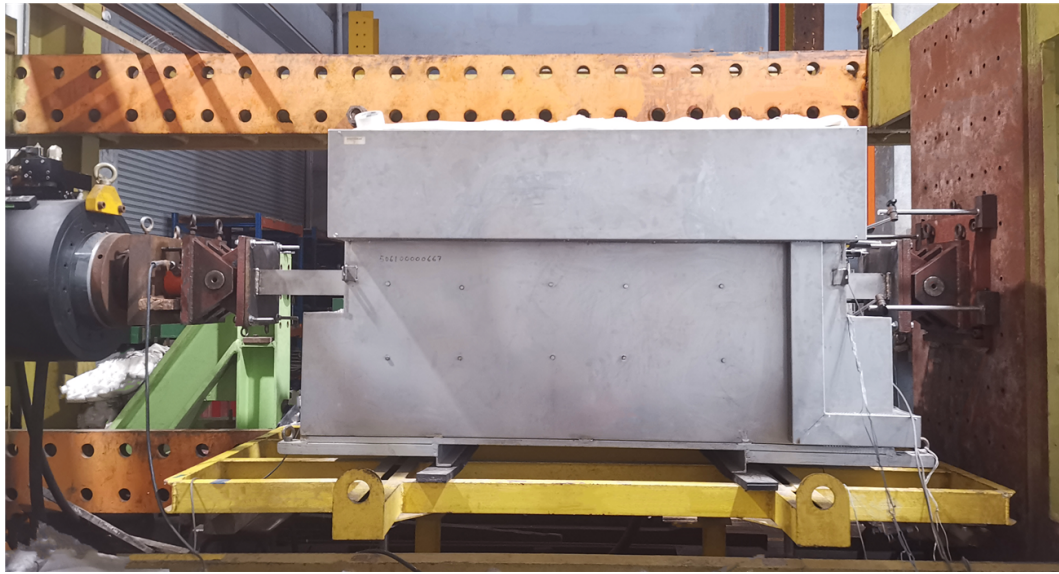
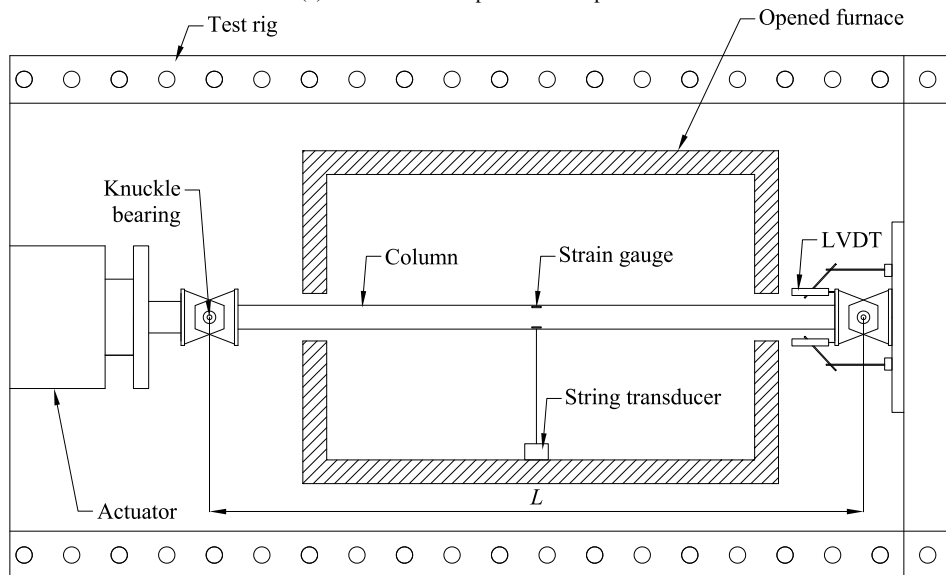


Figure 6: Stress-strain response of stainless steel at elevated temperatures determined using eqs. (3) and (4), based on the measured room temperature material properties and the elevated temperature reduction factors from [27], shown, as an example, for the 8 mm thick material



(a) Photo of test setup at room temperature



(b) Schematic drawing of room temperature column test setup

Figure 7: Column test setup at room temperature



Figure 8: Imperfection measurement setup

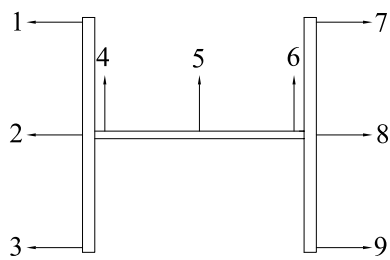
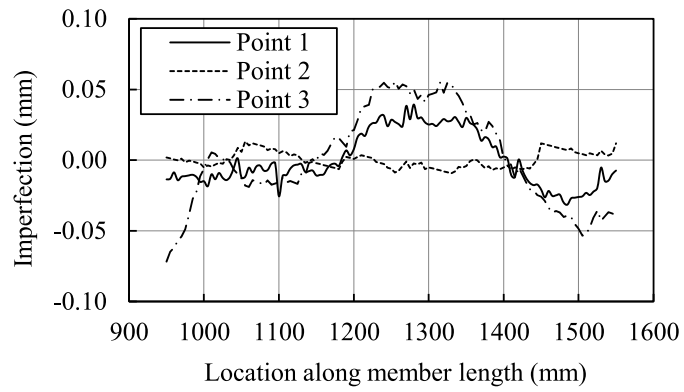
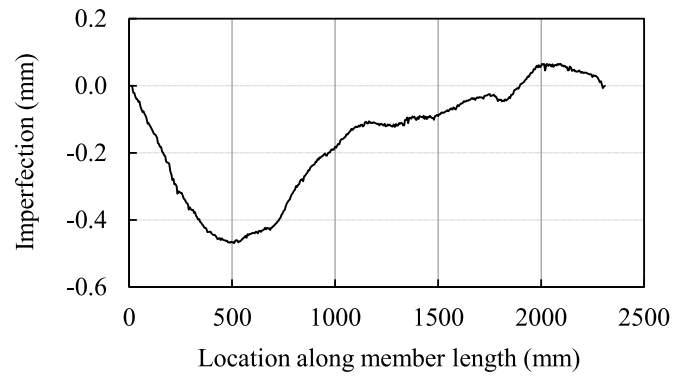


Figure 9: Imperfection measurement locations



(a) Local imperfection distributions for top flange



(b) Initial global imperfection distribution

Figure 10: Typical measured imperfection distributions; shown for specimen LC2-20C

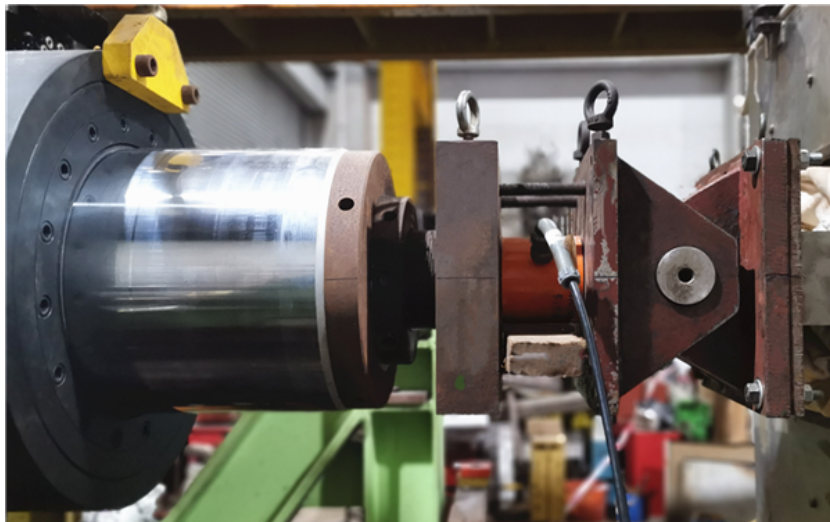


Figure 11: Details of loading system at column head

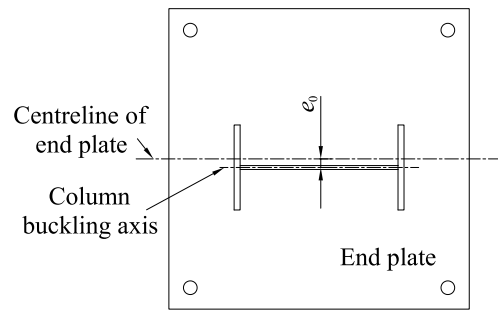


Figure 12: Positioning of specimens and end-plates

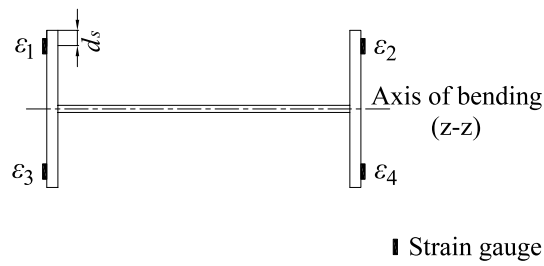


Figure 13: Strain gauge arrangement adopted at the mid-height of the specimens



Figure 14: Typical failure mode from room temperature tests, showing flexural buckling about the minor axis, illustrated for specimen LC2-20C

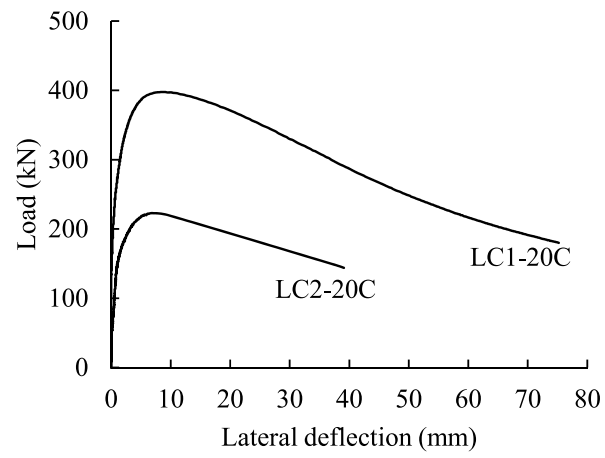
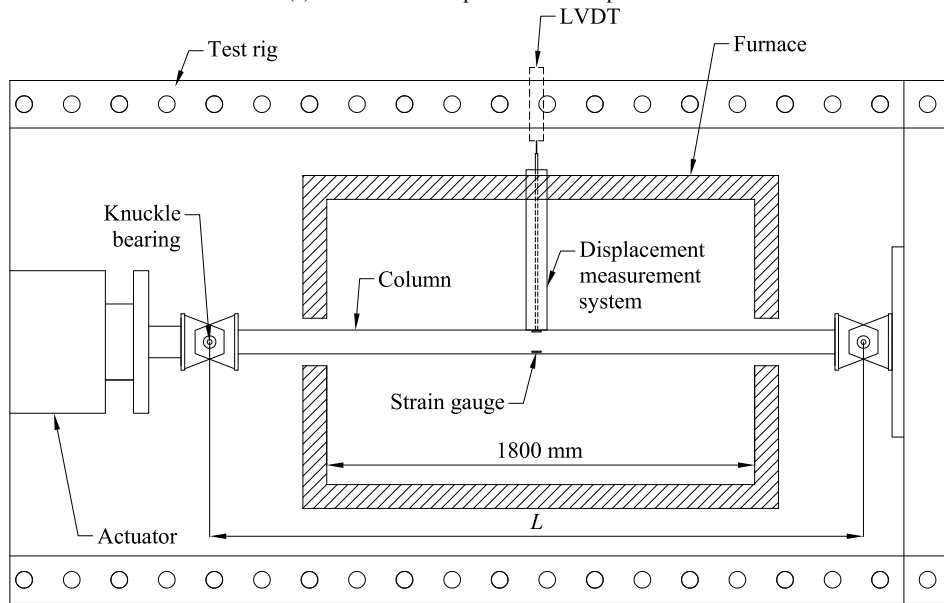


Figure 15: Load-mid-height lateral deflection curves for column tests at room temperature



(a) Photo of test setup at elevated temperature



(b) Schematic drawing of elevated temperature column test setup

Figure 16: Column test setup at elevated temperature

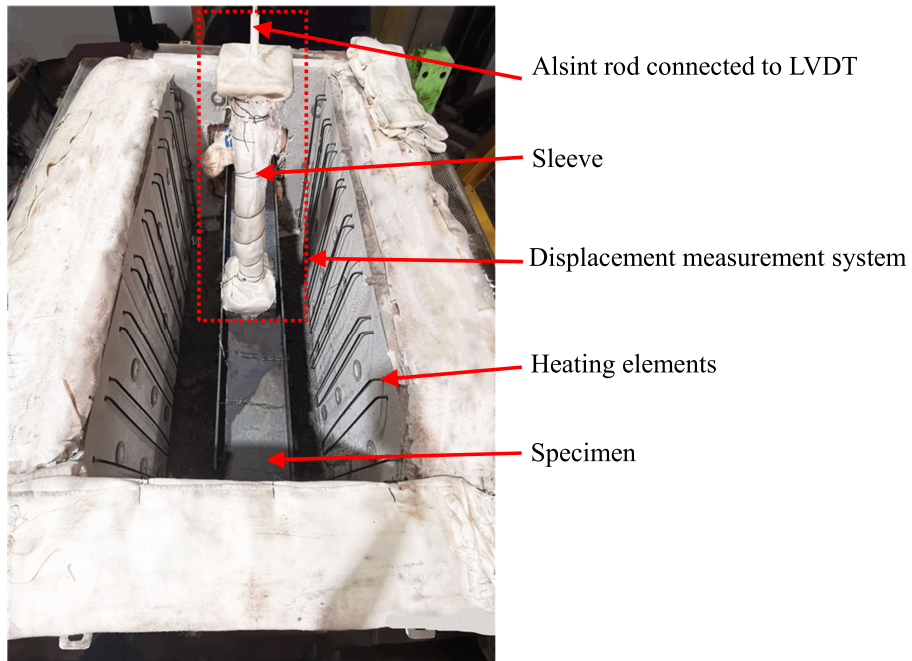


Figure 17: Inside of furnace used in fire tests

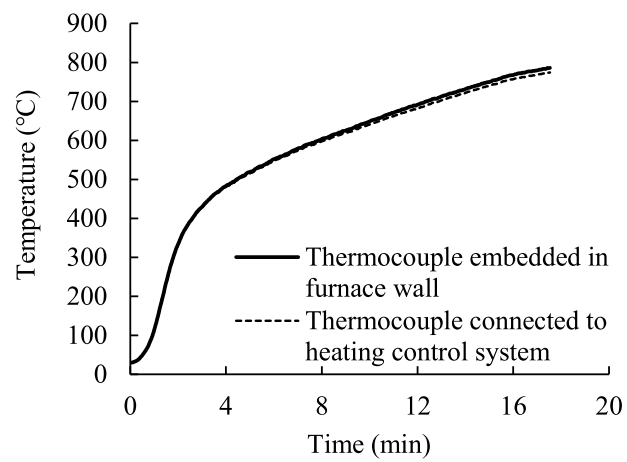


Figure 18: Furnace temperature measured by two thermocouples

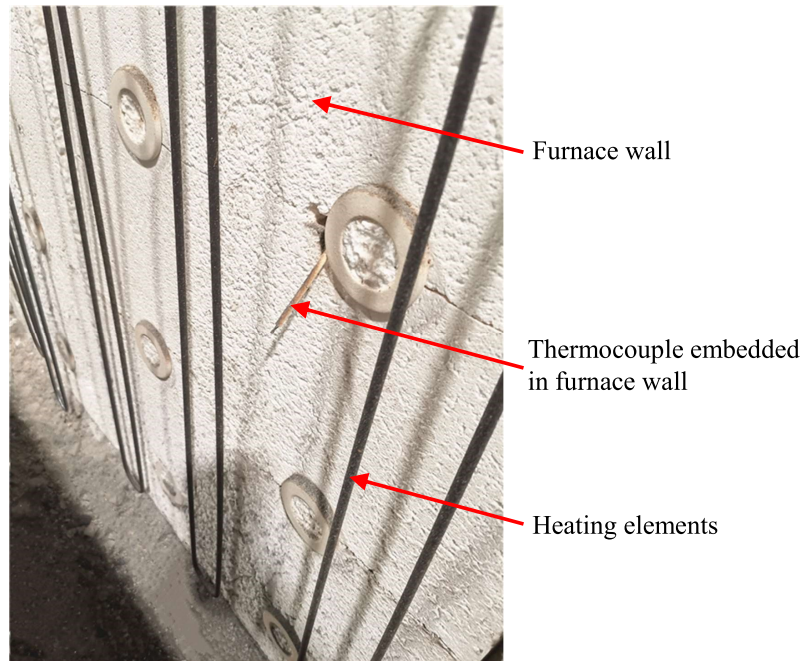


Figure 19: Thermocouple embedded in furnace wall

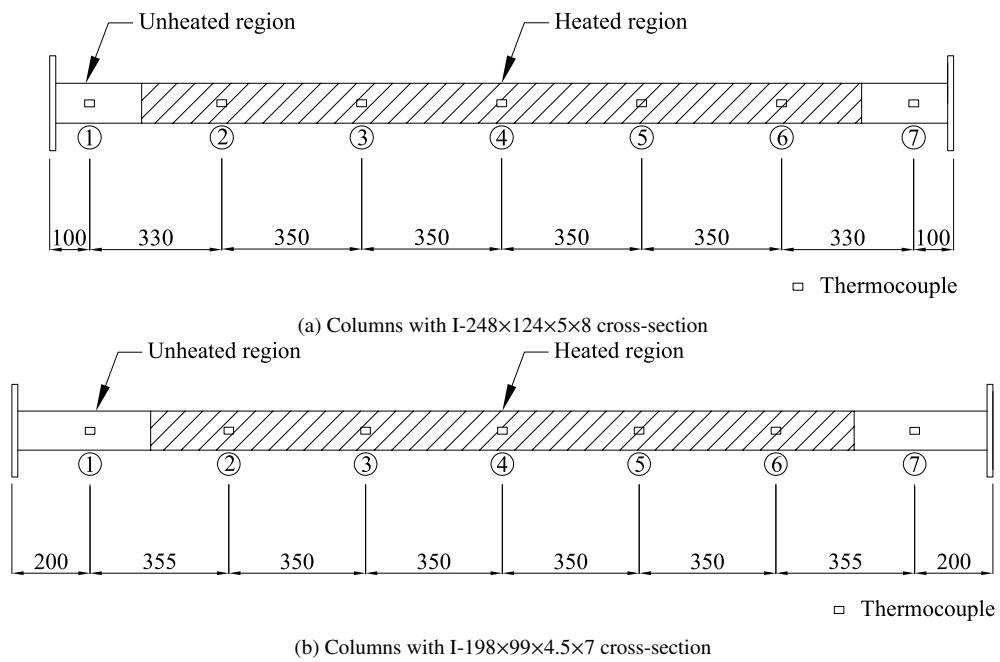


Figure 20: Locations of seven thermocouples on column specimens (dimensions in mm)

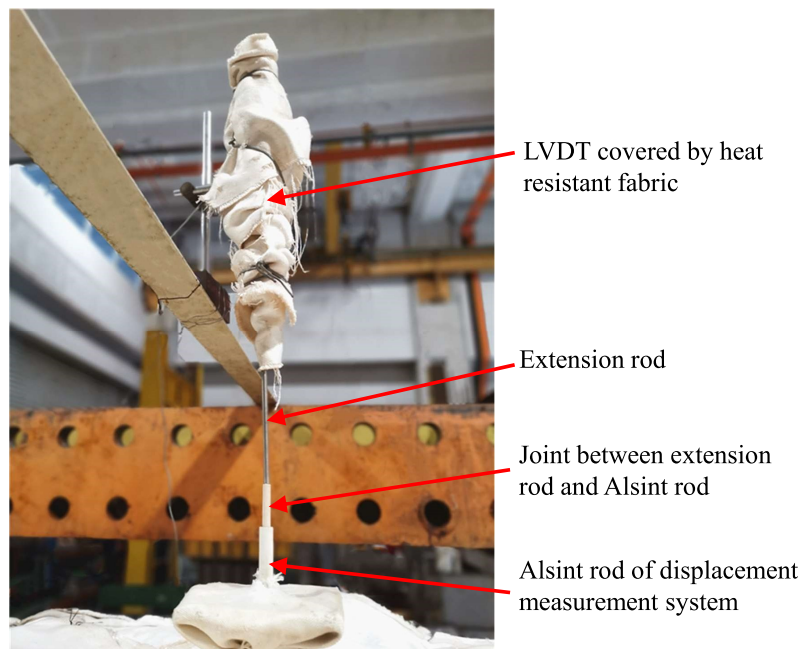
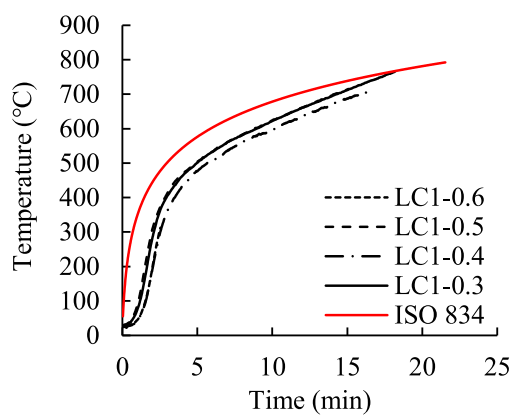


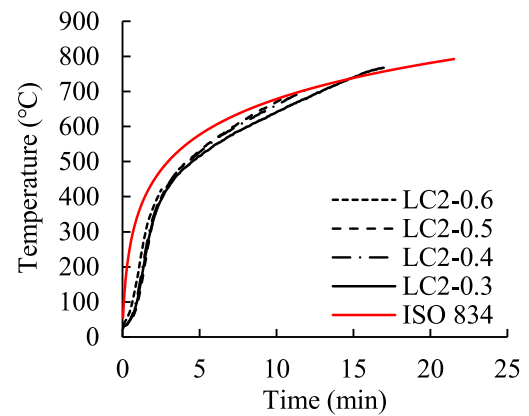
Figure 21: LVDT covered by heat resistant fabric used to measure mid-height lateral deflection of columns



Figure 22: Typical minor flexural buckling failure modes of specimens LC2-0.6, LC2-0.5, LC2-0.4, LC2-0.3 from top to bottom



(a) Columns with I-248×124×5×8 cross-section



(b) Columns with I-198×99×4.5×7 cross-section

Figure 23: Comparison of measured furnace temperature-time relationship with ISO-834 standard fire curve

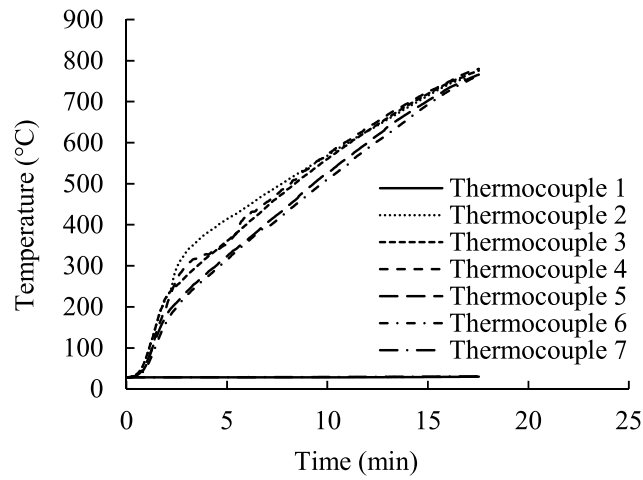
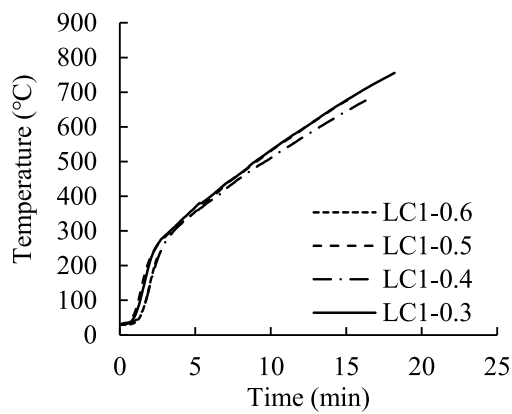
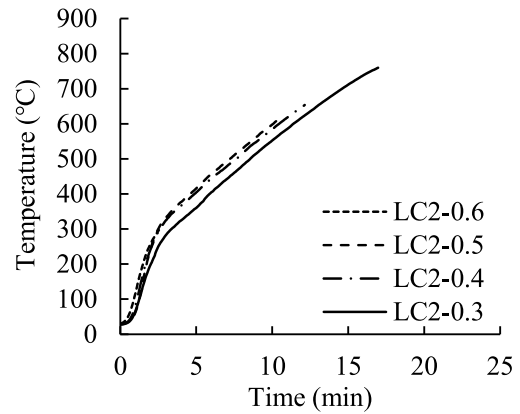


Figure 24: Temperature rise of column surface, shown for LC2-0.3

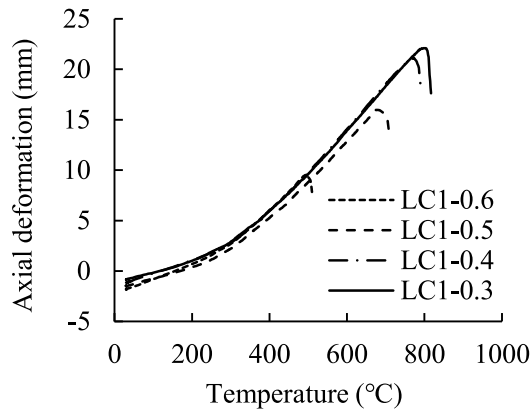


(a) Columns with I-248x124x5x8 cross-section

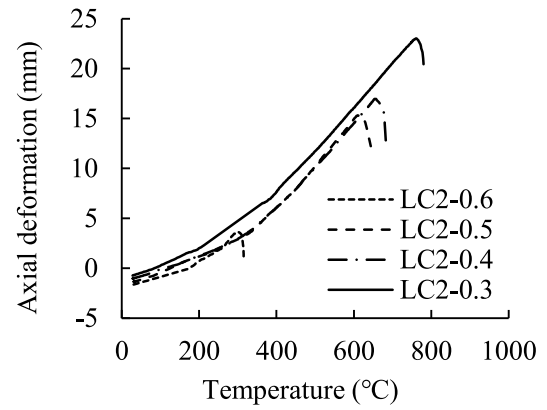


(b) Columns with I-198x99x4.5x7 cross-section

Figure 25: Average measured column surface temperature-time relationships for eight fire test specimens

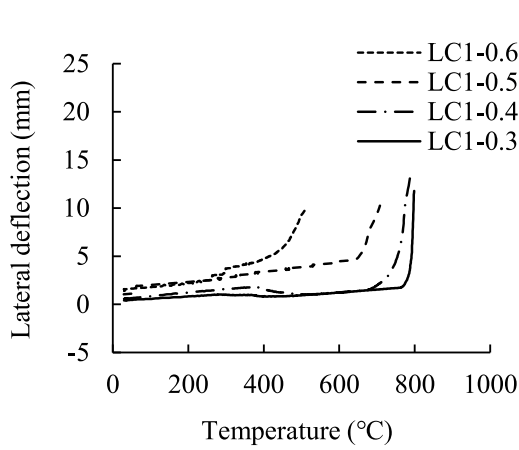


(a) Columns with I-248×124×5×8 cross-section

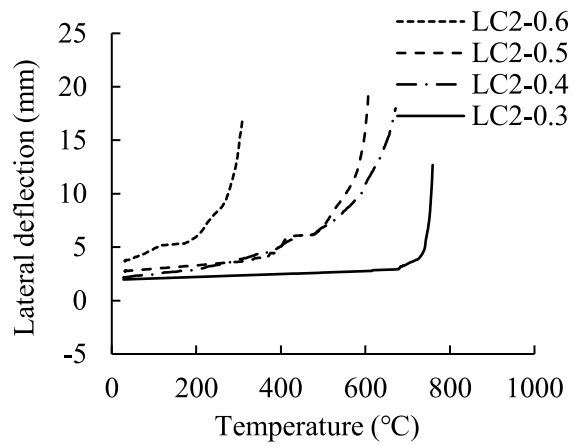


(b) Columns with I-198×99×4.5×7 cross-section

Figure 26: Axial deformation versus column temperature paths obtained from eight fire tests, with positive deformations corresponding to expansion of the columns



(a) Columns with I-248×124×5×8 cross-section



(b) Columns with I-198×99×4.5×7 cross-section

Figure 27: Mid-height lateral deflection versus column temperature paths obtained from eight column fire tests, with positive lateral deflections corresponding to downward deflections of the columns

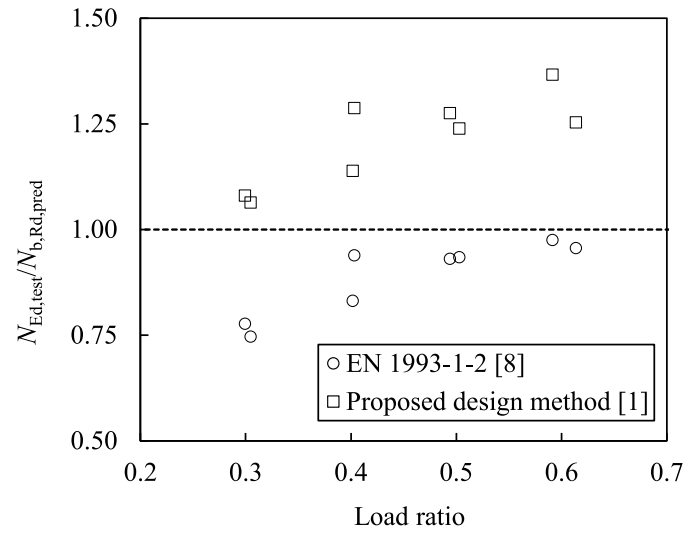


Figure 28: Comparison of buckling resistances in fire predicted by EN 1993-1-2 [20] and new proposal of Kucukler et al. [1] with test results

9. Tables

Table 1: Chemical compositions in mill certificates

Specimen	Material grade	C (%)	Si (%)	Mn (%)	P (%)	S (%)	Ni (%)	Cr (%)	N (%)
I-198×99×4.5×7	1.4301	0.026	0.41	1.37	0.032	0.001	8.00	18.01	0.070
		0.024	0.40	1.38	0.031	0.002	8.05	18.05	0.069
I-248×124×5×8	1.4301	0.026	0.41	1.37	0.032	0.001	8.00	18.01	0.070
		0.021	0.22	1.77	0.038	0.003	8.08	18.32	-

Table 2: Material properties in mill certificates

Specimen	$f_{y, \text{mill}}$ (N/mm ²)	$f_{p1.0, \text{mill}}$ (N/mm ²)	$f_{u, \text{mill}}$ (N/mm ²)	$\varepsilon_{f, \text{mill}}$ (%)
I-198×99×4.5×7	312	349	630	51
	313	348	625	52
I-248×124×5×8	312	349	630	51
	329	-	612	52

Table 3: Key material properties obtained from tensile coupon tests

ID	t (mm)	E (N/mm ²)	f_y (N/mm ²)	$f_{p1.0}$ (N/mm ²)	$f_{2.0}$ (N/mm ²)	f_u (N/mm ²)	ε_u (%)	ε_f (%)	R-O coefficient	
TC4.5-W-1	4.83	198200	324	386	405	688	57	70	4.7	2.8
TC4.5-W-2	4.87	194600	298	376	399	681	55	69	5.5	3.2
TC5-W-1	4.88	194800	297	377	396	674	54	69	5.4	2.8
TC5-W-2	4.85	197700	306	386	407	685	55	72	5.2	2.9
TC7-F-1	6.92	193700	263	320	356	665	57	74	5.7	2.8
TC7-F-2	6.93	198800	254	323	343	649	54	77	6.7	2.6
TC8-F-1	7.99	202700	324	375	395	691	54	78	5.9	2.5
TC8-F-2	8.01	202000	347	397	416	707	58	81	5.8	2.5

Table 4: Geometric properties and imperfections of tested stainless steel I-section column specimens

ID	Cross-section	L (mm)	h (mm)	b (mm)	t_w (mm)	t_f (mm)	w_f (mm)	w_w (mm)	w_0 (mm)	v_0 (mm)
LC1-20C	I-248×124×5×8	2502.25	248.27	124.43	4.90	8.03	0.08	0.07	0.08	0.32
LC1-0.6	I-248×124×5×8	2502.20	248.46	124.44	4.91	8.05	0.05	0.06	0.06	0.15
LC1-0.5	I-248×124×5×8	2502.60	248.23	124.45	4.90	8.06	-	-	-	0.35
LC1-0.4	I-248×124×5×8	2501.75	248.45	124.45	4.96	8.05	-	-	-	0.23
LC1-0.3	I-248×124×5×8	2502.50	248.31	124.52	5.00	8.03	-	-	-	0.30
LC2-20C	I-198×99×4.5×7	2751.75	198.12	99.47	4.88	6.94	0.07	0.05	0.07	0.47
LC2-0.6	I-198×99×4.5×7	2752.20	198.22	99.45	4.67	6.92	0.04	0.04	0.04	0.39
LC2-0.5	I-198×99×4.5×7	2752.25	198.04	99.44	4.92	6.89	-	-	-	0.35
LC2-0.4	I-198×99×4.5×7	2752.50	198.32	99.47	4.95	6.95	-	-	-	0.39
LC2-0.3	I-198×99×4.5×7	2752.60	198.21	99.49	4.77	7.02	-	-	-	0.44

Table 5: Key experimental results of column tests at room temperature

ID	Cross-section	Total global imperfection $v_0 + e_0$ (mm)	Ultimate load N_u (kN)	Lateral displacement at N_u (mm)	End rotation at N_u (rad)
LC1-20C	I-248×124×5×8	2.42	398	8.8	0.72
LC2-20C	I-198×99×4.5×7	1.03	223	7.0	0.32

Table 6: Measured imperfections, pre-applied axial loads and load ratios of columns subjected to fire testing

ID	Cross-section	Total global imperfection $v_0 + e_0$ (mm)	Pre-applied load $N_{Ed,test}$ (kN)	Load ratio n_r
LC1-0.6	I-248×124×5×8	2.47	248	0.62
LC1-0.5	I-248×124×5×8	2.38	203	0.51
LC1-0.4	I-248×124×5×8	2.04	160	0.40
LC1-0.3	I-248×124×5×8	2.29	119	0.30
LC2-0.6	I-198×99×4.5×7	2.74	137	0.61
LC2-0.5	I-198×99×4.5×7	2.37	110	0.49
LC2-0.4	I-198×99×4.5×7	2.71	97	0.43
LC2-0.3	I-198×99×4.5×7	2.52	68	0.30

Table 7: Measured fire resistances from column tests

ID	Fire resistance $t_{fi,test}$ (min)	Critical temperature $\theta_{cr,test}$ (°C)
LC1-0.6	9.27	488
LC1-0.5	15.07	676
LC1-0.4	20.57	770
LC1-0.3	24.43	799
LC2-0.6	2.53	297
LC2-0.5	10.30	609
LC2-0.4	12.13	654
LC2-0.3	16.97	760

Table 8: Column buckling resistances in fire predicted by EN 1993-1-2 [20]

ID	θ_{cr} (°C)	Pre-applied load $N_{Ed,test}$ (kN)	Predicted buckling resistance $N_{b,Rd,EC3}$ at θ_{cr} (kN)	$N_{Ed,test}/N_{b,Rd,EC3}$
LC1-0.6	488	248	259	0.96
LC1-0.5	676	203	217	0.93
LC1-0.4	770	160	171	0.94
LC1-0.3	799	119	153	0.78
LC2-0.6	297	137	140	0.98
LC2-0.5	609	110	118	0.93
LC2-0.4	654	97	116	0.83
LC2-0.3	760	68	91	0.75
Average				0.89
COV				0.099

Table 9: Column buckling resistances in fire predicted by new proposed method [1]

ID	θ_{cr} (°C)	Pre-applied load $N_{Ed,test}$ (kN)	Predicted buckling resistance $N_{b,Rd,Prop}$ at θ_{cr} (kN)	$N_{Ed,test}/N_{b,Rd,Prop}$
LC1-0.6	488	248	198	1.25
LC1-0.5	676	203	164	1.24
LC1-0.4	770	160	125	1.29
LC1-0.3	799	119	110	1.08
LC2-0.6	297	137	100	1.37
LC2-0.5	609	110	86	1.28
LC2-0.4	654	97	85	1.14
LC2-0.3	760	68	64	1.06
Average				1.21
COV				0.088

Table 10: Comparison of finite element results from the full-heated column models and part-heated column models

ID	Critical temperature (°C)	$N_{u,FE,full-heated}$ (kN)	$N_{u,FE,part-heated}$ (kN)	$N_{u,FE,part-heated}/N_{u,FE,full-heated}$
LC1-0.6	488	241	244	1.01
LC1-0.5	676	201	204	1.01
LC1-0.4	770	159	160	1.01
LC1-0.3	799	142	145	1.03
LC2-0.6	297	119	122	1.03
LC2-0.5	609	97	99	1.03
LC2-0.4	654	91	92	1.01
LC2-0.3	760	73	75	1.04
Average				1.02
COV				0.010

Table 11: Comparison of finite element results from the column models with and without considering self-weight

ID	Critical temperature (°C)	$N_{u,FE,w}$ (kN)	$N_{u,FE,nw}$ (kN)	$N_{u,FE,w}/N_{u,FE,nw}$
LC1-0.6	488	243	244	1.00
LC1-0.5	676	202	204	0.99
LC1-0.4	770	157	160	0.98
LC1-0.3	799	142	145	0.98
LC2-0.6	297	121	122	0.99
LC2-0.5	609	97	99	0.98
LC3-0.4	653	90	92	0.98
LC2-0.3	760	73	75	0.97
Average				0.99
COV				0.009